

Exchange and correlation effects on the plasmon dispersions and the Coulomb drag in low-density electron bilayers

S. M. Badalyan,^{1,*} C. S. Kim,¹ and G. Vignale²

¹*Department of Physics and Institute for Condensed Matter Theory,*

Chonnam National University, Gwangju 500-757, Korea

²*Department of Physics and Astronomy,*

University of Missouri - Columbia, Missouri 65211, USA

(Dated: December 2, 2024)

Abstract

We investigate the effect of exchange and correlation (xc) on the Coulomb drag between spatially separated low-density two-dimensional electron layers. The novel feature of our approach is that we make use of dynamic xc kernels for the calculation of the bilayer plasmon dispersions and of the drag mediated by exchange of these plasmons. On the other hand, the particle-hole contribution to the transresistivity is still calculated with the help of static many-body local field factors. The spectrum of bilayer plasmons and the drag transresistivity are calculated in a broad range of temperatures taking into account both intra- and inter-layer correlation effects. We find that the introduction of xc corrections results in a significant enhancement of the transresistivity and qualitative changes in its temperature dependence. In particular, the large high-temperature plasmon peak that is present in the random phase approximation is found to disappear when the xc corrections are included. Our numerical results are in reasonable agreement with the results of recent experiments.

PACS numbers: 71.45.Gm, 73.20.Mf, 73.63.Hs

I. INTRODUCTION

In a double layer two-dimensional electron system (2DES) the additional degree of freedom associated with the layer index plays a key role in many recently discovered collective phenomena¹. Suffice it to mention the freshly provided evidence that in the quantum Hall regime, near the half filling of individual layers, strong electron-hole inter-layer correlations cause Bose-Einstein condensation of excitons to occur in bilayer 2D electron and hole systems². In these structures, the ability to make separate electrical contacts to each layer has allowed the experimental detection of transport of neutral excitons as a counter-flowing current of electrons and holes in two layers. The independent control of layers is also critical for the experimental realization of the frictional drag³ which manifests itself under the condition that the second layer is an open circuit. A current driven along the first layer induces, via momentum transfer, a voltage in the second layer, which is measured experimentally. The drag effect complements and enriches the traditional experimental methods and in the last decade has proved to be a powerful tool to probe inter-layer electron-electron (e-e) interaction⁴.

Recently the drag measurements have been extended to the limit of very low carrier concentration. The dimensionless parameter $r_s = \sqrt{2}/(k_F a_B^*)$, which describes the carrier density, n , and measures the strength of the electron-electron interaction⁵, varies approximately from 10 to 20 in the experiment on hole samples by Pillarisetty *et al.*^{6,7}. Here $k_F = \sqrt{2\pi n}$ is the Fermi wave vector, and $a_B^* = \hbar^2 \kappa_0 / m^* e^2$ is the effective Bohr radius, with κ_0 the static dielectric constant and m^* the effective mass of the carriers; $a_B^* = 9.79$ and 1.73 nm, respectively, in the conduction and valence bands of GaAs. In the experiment on electron samples by Kellogg *et al.*⁸, r_s is appreciably smaller, owing to the small effective mass of the electrons. From a dimensional analysis it is clear, however, that in both types of samples, the Coulomb potential energy dominates the kinetic energy, and an adequate description of the drag cannot be provided by simple theories, which do not include the strong exchange-correlation (xc) effects. Consistent with this expectation, both experimental groups^{6,8} have found that the measured drag rate far exceeds (by more than a factor 200 in the hole samples) the value obtained from simple Boltzmann-equation calculations⁹. In addition, systematic deviations are observed from the quadratic temperature dependence of the drag rate (the characteristic Fermi-liquid behavior of the Coulomb drag at low temper-

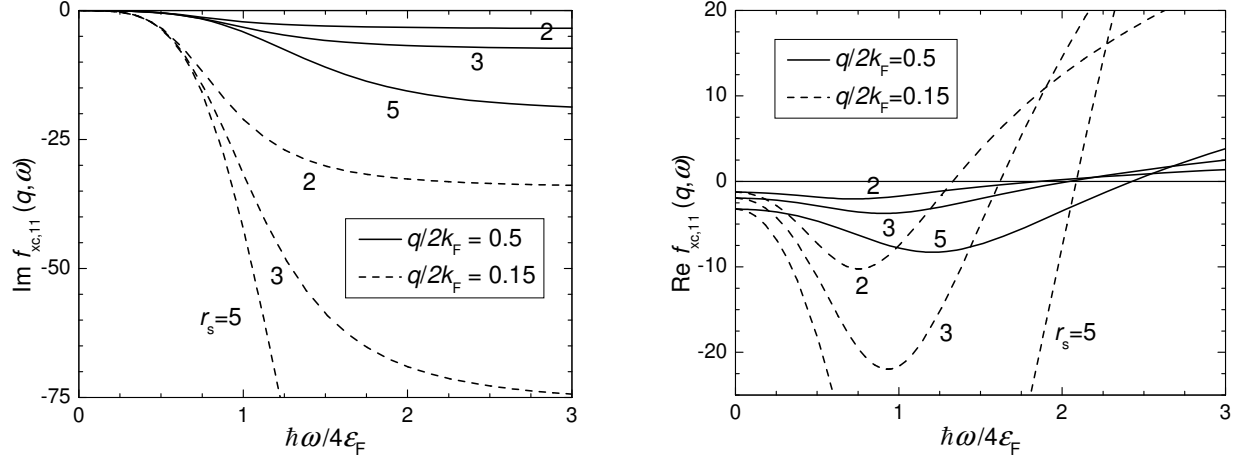


FIG. 1: Imaginary part (figure on the left) and real part (figure on the right) of the intra-layer dynamic xc kernel, $f_{\text{xc},11}(q, \omega)$, of a bilayer 2DES as a function of ω . The kernels are shown for $r_s = 2, 3$, and 5 and for two different values of the wave vector q in the units of g_0^{-1} where $g_0 = m^*/\pi\hbar^2$ is the density of states for the noninteracting 2DES.

atures).

One might hope that the above features could be understood in the framework of the phonon-mediated drag mechanism^{10,11,12,13,14,15,16}. However, the phonon-mediated drag provides a dominant mechanism only in samples with large inter-layer spacing where the absolute value of the measured drag rate is much smaller than that observed in these experiments. Moreover, the phonon mechanism is not supported by the measured density-ratio-dependence of drag⁶, which shows no peak at matched carrier densities in two layers, typical for that processes. Thus, both experimental groups^{6,8} conclude that in these dilute 2DES the strong Coulomb interaction effects are mainly responsible for the observed new features.

The carrier interaction effects on drag have been addressed previously in several experimental^{17,18,19} and theoretical^{20,21,22} papers. While the theoretical prediction by Flensberg and Hu²¹ of a strong enhancement of drag by plasmons has been experimentally verified¹⁸ in high density electron samples, important differences have been reported¹⁹ from the results obtained within the random phase approximation (RPA).

Lately, motivated by the recent set of low-density experiments^{6,8}, the drag transresistivity has been calculated by Hwang *et al.*²³ and Yurtserver *et al.*²⁴. Both works have included only the exchange interaction effects in the static limit via q -dependent but ω -independent

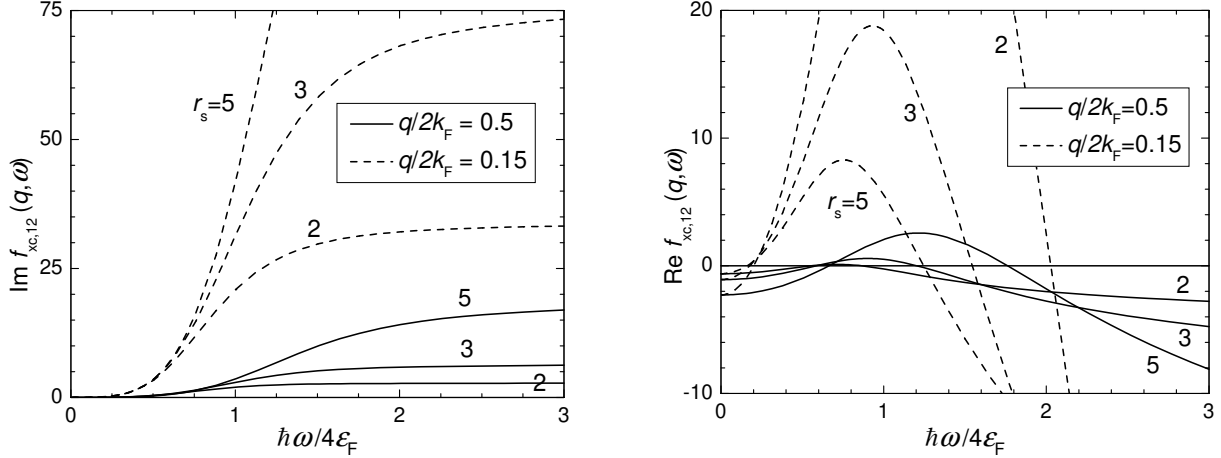


FIG. 2: Imaginary parts (figure on the left) and real part (figure on the right) of the inter-layer dynamic xc kernel, $f_{xc,12}(q, \omega)$, of a bilayer 2DES as a function of ω . The kernels are shown for $r_s = 2, 3$, and 5 and for two different values of the wave vector q in the units of g_0^{-1} where $g_0 = m^*/\pi\hbar^2$ is the density of states of the noninteracting 2DES.

local field factors (LFF). Besides, in the adopted approximation the nondiagonal inter-layer LFF have been taken to be zero²³, while for the intra-layer LFF the simple Hubbard approximation has been used, which significantly underestimates the LFF. As in the low density regime the inter-particle spacing in each layer becomes comparable with the inter-layer separation, one should expect that inter-layer correlations play an important role. At relatively high temperatures the dynamic xc effects are also critical. They can be especially important in the hole samples where, even at sufficiently low temperatures, the samples are effectively in the high temperature regime because of the small Fermi energy.

In this paper we investigate the xc effects on the Coulomb drag in low-density coupled 2DES. The spectrum of bilayer plasmons and the temperature dependence of the drag transresistivity are calculated in a broad range of temperatures. Our calculations include both intra- and inter-layer xc effects. We propose a new approach, which employs dynamic xc kernels in the calculation of the bilayer plasmon spectra and of the plasmon-mediated drag, while the particle-hole contribution to the drag is still calculated by means of static many-body LFF. We find that the introduction of xc corrections results in a significant enhancement of the drag transresistivity and qualitative changes in its temperature dependence. In particular, a large high-temperature plasmon peak that is present in the RPA disappears when the xc corrections are included. Our numerical results are in reasonable

agreement with the experimental findings by Kellogg *et al.*⁸.

The paper is organized as follows. In Section II we outline the theoretical formulation of the frictional drag and provide the main formulas for its calculation beyond the RPA. In Section III the dynamic xc kernels and the static many-body LFF of the bilayer 2DES are presented. The results of actual calculations are given in Sections IV-VI. First we present the spectra of bilayer plasmons for different densities and discuss the effect of dynamic xc on the dispersion of each plasmon mode, comparing the dispersion curves with the corresponding curves obtained within the RPA. In Section V we study the temperature dependence of the drag transresistivity at low densities within the RPA. Both plasmon and particle-hole contributions to the drag are considered. In the next section we investigate the many-body xc effects on the drag transresistivity for different densities and examine the distinctive features of the drag temperature dependence in comparison with the RPA. Finally, Section VII summarizes the main results of the paper.

II. THEORETICAL FORMULATION

We calculate the temperature dependence of the drag transresistivity starting from the formula, obtained in the Kubo formalism²⁵

$$\rho_D = \frac{\hbar^2}{2e^2\sigma_1\sigma_2TA} \frac{d\sigma_1}{dn_1} \frac{d\sigma_2}{dn_2} \sum_{\vec{q}} q^2 \int_0^\infty \frac{d\omega}{2\pi} |W_{12}(q, \omega)|^2 \times \frac{\text{Im}\Pi_1^0(q, \omega)\text{Im}\Pi_2^0(q, \omega)}{\sinh^2(\hbar\omega/2T)}, \quad (1)$$

where A is the normalization area, $\hbar\omega$ and $\hbar\vec{q}$ the transferred energy and in-plane momentum from the layer 1 to the layer 2, $W_{12}(q, \omega)$ the dynamically screened inter-layer e-e interaction including the intra- and inter-layer many-body xc effects of a bilayer 2DES, $\Pi_{1,2}^0(q, \omega)$ the finite temperature electron polarization function of an individual 2DES in the absence of inter-particle Coulomb interaction. The imaginary and real parts of $\Pi_{1,2}^0(q, \omega)$ are obtained from the Maldague formula^{21,26} and are given by

$$\text{Im}\Pi^0(q, \omega) = \frac{\sqrt{\pi t}}{4x} \left[F_{-1/2} \left(\frac{\mu(t) - \zeta_+^2(x, y)}{t} \right) - F_{-1/2} \left(\frac{\mu(t) - \zeta_-^2(x, y)}{t} \right) \right], \quad (2)$$

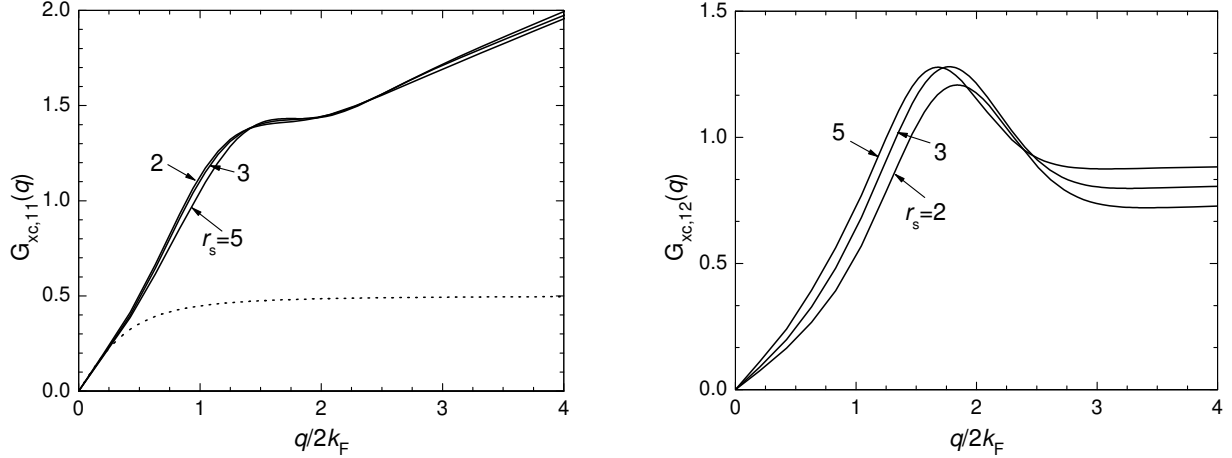


FIG. 3: Static many-body LFF of a double layer 2DES. The intra-layer, $G_{xc,11}$ (figure on the left), and the inter-layer, $G_{xc,12}$ (figure on the right), are plotted as functions of wave vector q for equal electron densities in the two layers corresponding to $r_s = 2, 3$, and 5 . The dotted curve shows the LFF in the Hubbard approximation.

and

$$\begin{aligned} \text{Re}\Pi^0(q, \omega) = & 1 - e^{-1/t} - \frac{1}{2x} [M(t, \zeta_+^2(x, y)) \\ & - \text{sign}(\zeta_-(x, y)) M(t, \zeta_-^2(x, y))] , \end{aligned} \quad (3)$$

where we have introduced the following dimensionless quantities: $t = T/\varepsilon_F$, $x = q/2k_F$, $y = \omega/4\varepsilon_F$, $\mu(t) = t \ln(e^{1/t} - 1)$, $\zeta_{\pm}(x, y) = y/x \pm x$ with ε_F and k_F being the Fermi energy and the Fermi wave vector. Here

$$F_{-1/2}(u) = 1/\sqrt{\pi} \int_0^\infty dz/\sqrt{z} (\exp(z - u) + 1) \quad (4)$$

is the Fermi integral, and

$$M(t, u) = 1/4t \int_0^u dz \sqrt{u - z} / \cosh [(z - \mu(t))/2t]^2 . \quad (5)$$

Further we assume that in Eq. (1) the layer conductivities $\sigma_{1,2}$ depend linearly on the electron densities $n_{1,2}$. In general, this is an acceptable approximation for the conducting 2DES in the magnetic-field-free case. Deviations from the linear regime can occur at low electron densities. Here we are interested in the regime corresponding to $r_s \leq 5$; yet even in this regime we expect that the neglect of the corrections to the $\sigma_{1,2} \propto n_{1,2}$ remains a reasonable approximation.

Our starting equation (1) is an approximation, strictly justifiable only to second order in the Coulomb interaction. The correct expression for the transresistivity involves a force-force response function, which is a four-point response function and cannot be reduced, in general, to a product of two two-point response functions. Therefore, in the adopted approximation, the form of the interlayer interaction is not determined uniquely. In order to include the xc effects on the dynamically screened interlayer Coulomb interaction, in our calculations we have exploited two different approximations for W_{12} . Within the first scheme, developed by Vignale and Singwi²⁷, a matrix Dyson equation for the exact Coulomb propagator $\hat{W}(q, \omega)$ is approximated by

$$\hat{W}(q, \omega) = \hat{v}(q) + \hat{V}_{\text{eff}}(q, \omega) \hat{\Pi}(q, \omega) \hat{V}_{\text{eff}}(q, \omega) \quad (6)$$

with the full polarization function, $\hat{\Pi}(q, \omega)$, defined in terms of the unscreened effective Coulomb interactions, $\hat{V}_{\text{eff}}(q, \omega)$, as

$$\hat{\Pi}(q, \omega) = \frac{\hat{\Pi}_0(q, \omega)}{1 - \hat{V}_{\text{eff}}(q, \omega) \hat{\Pi}_0(q, \omega)}. \quad (7)$$

Here all quantities are 2×2 matrices. Thus, the non-diagonal interaction matrix element $W_{12}(q, \omega)$ in this scheme is given by

$$W_{12}(q, \omega) = \frac{V_{\text{eff},12}(q, \omega)}{\varepsilon_{\text{bi}}(q, \omega)} + v(q) G_{\text{xc},12}(q, \omega) F_{12}(qd, q\Lambda), \quad (8)$$

with the bilayer screening function

$$\varepsilon_{\text{bi}}(q, \omega) = \varepsilon_1(q, \omega) \varepsilon_2(q, \omega) - V_{\text{eff},12}(q, \omega)^2 \Pi_1^0(q, \omega) \Pi_2^0(q, \omega). \quad (9)$$

Here we introduce the screening functions of individual layers

$$\varepsilon_{1,2}(q, \omega) = 1 + V_{\text{eff},11,22}(q, \omega) \Pi_{1,2}^0(q, \omega). \quad (10)$$

The intra- and inter-layer unscreened effective Coulomb interactions are given by

$$V_{\text{eff},ij}(q, \omega) = v(q) (1 - G_{\text{xc},ij}(q, \omega)) F_{ij}(qd, q\Lambda) \quad (11)$$

where the intra- and inter-layer LFF $G_{\text{xc},ij}(q, \omega)$ decrease effectively the bare Coulomb interaction, $v(q) = 2\pi e^2/\kappa_0 q$, by a factor of $1 - G_{\text{xc},ij}(q, \omega)$ ($i, j = 1, 2$ are the layer indices). Further we assume that the electrons in each layer are confined by a square well potential of infinite height and that scattering processes take place only within the lowest subband of

each wells. Making use $\rho_1(z) = (2/d) \sin(\pi z/d)^2$ and $\rho_2(z) = \rho_1(z + \Lambda)$ as explicit forms for the electron density profiles in layers 1 and 2, respectively, one obtains⁹ for the corresponding intra- and inter-layer form factors in Eq. 11

$$F_{11}(\eta, \xi) = \frac{8\pi^2 + 3\eta^2}{\eta(4\pi^2 + \eta^2)} - \frac{32\pi^4(1 - e^{-\eta})}{\eta^2(4\pi^2 + \eta^2)^2} \quad (12)$$

and

$$F_{12}(\eta, \xi) = \frac{64\pi^4 \sinh(\eta/2)^2}{\eta^2(4\pi^2 + \eta^2)^2} e^{-\xi}, \quad (13)$$

where Λ is the center-to-center inter-layer separation and d the width of quantum wells.

Within the second scheme, proposed by Zheng and MacDonald²⁸ (see also Ref. 22), a matrix Dyson equation for the dynamically screened Coulomb interaction $\hat{W}(q, \omega)$ is approximated by

$$\hat{W}(q, \omega) = \hat{V}_{\text{eff}}(q, \omega) + \hat{V}_{\text{eff}}(q, \omega) \hat{\Pi}(q, \omega) \hat{V}_{\text{eff}}(q, \omega) \quad (14)$$

which corresponds to the inter-layer interaction

$$W_{12}(q, \omega) = \frac{V_{\text{eff},12}(q, \omega)}{\varepsilon_{\text{bi}}(q, \omega)} \quad (15)$$

where the xc LFF manifest themselves only via the effective interactions (11). Notice that the RPA is recovered if all the LFF in Eqs. 8 and 15 are set to zero.

III. DYNAMIC XC KERNEL AND STATIC LFF

We interpret the layer index as an isospin²⁹ and represent the intra- and inter-layer LFF of the bilayer 2DES in terms of the "spin-channel" and "charge-channel" LFF, denoted respectively by $G_{\text{xc}}^-(q, \omega)$ and $G_{\text{xc}}^+(q, \omega)$ in the following manner:

$$\begin{aligned} G_{\text{xc},11}(q, \omega) &= G_{\text{xc}}^+(q, \omega) + G_{\text{xc}}^-(q, \omega), \\ G_{\text{xc},12}(q, \omega) &= G_{\text{xc}}^+(q, \omega) - G_{\text{xc}}^-(q, \omega). \end{aligned} \quad (16)$$

Of course this simple representation is possible only in the symmetric case, $n_1 = n_2$. Notice that the above approach has certain limitations. Despite the full xc kernels, $f_{\text{xc},ij}(q, \omega | d, \Lambda) \equiv -v(q)G_{\text{xc},ij}(q, \omega)F_{ij}(qd, q\Lambda)$, show correct asymptotic behavior as a function of inter-layer spacing, the LFF remain independent of spacing when the two layers are far apart. This makes the off-diagonal LFF $G_{\text{xc},12}$ unreliable in this limit. According to the experimental

situation of interest here, which shows no spin signature, we have ignored the spin effects in treating the bilayer LFF. Thus, the adopted approach does not account for the valley degeneracy when the layers are very close. This approximation is also justified in the view of the fact that the inter-layer LFF arise from a correlation effect, which should be insensitive to the relative spin orientation of the electrons in the two layers.

When treating the plasmon contribution to the Coulomb drag in our calculations we approximate the dynamic xc kernels, $f_{\text{xc},ij}(q, \omega) \equiv -v(q)G_{\text{xc},ij}(q, \omega)$, by their long-wavelength limits and employ the dynamic spin-spin and charge-charge xc kernels, evaluated by Qian and Vignale in Refs. 30 and 31. In this way we include the frequency dependence of the dynamic charge-charge LFF, while their wave vector dependence tacitly assumed to be linear so that the charge-charge xc kernel is independent of q . This is a reasonable approximation in view of the nearly linear behavior of the exact static LFF versus q in the single layer⁵. On the other hand, the spin-spin dynamic xc kernel is strongly dependent on q and diverges as q^{-2} at small wave vectors³². Thus, the intra- and inter-layer dynamic xc kernels in the long wavelength limit are represented as

$$f_{\text{xc},ij}(q, \omega) = B^+(\omega) + (2\delta_{ij} - 1) \left[\frac{A(\omega)}{q^2} + B^-(\omega) \right] \quad (17)$$

where $A(\omega)$ and $B^\pm(\omega)$ are finite functions of ω and have been calculated to the leading order in the Coulomb interaction in Refs. 30 and 31. The authors of this paper have evaluated the four-vertex diagrams in the expansion of the response function of individual 2DES in the low-frequency/high-density limit. The interpolation formulas for $\text{Im } A(\omega)$ and $\text{Im } B^\pm(\omega)$ have been constructed by combining the results for the imaginary parts with sum rules and previously known exact behaviors in the high-frequency limit³³. Thus, having the imaginary parts of $A(\omega)$ and $B^\pm(\omega)$, one can obtain the corresponding real parts from the Kramers-Kroning relations.

Figs. 1 and 2 show plots of the imaginary and real parts of the intra- and inter-layer xc kernels, $f_{\text{xc},11}(q, \omega)$ and $f_{\text{xc},12}(q, \omega)$, which we actually use in our calculations of the spectrum of bilayer plasmons and of the Coulomb drag mediated by these plasmons. At finite frequencies, the term in Eq. 17, related to $A(\omega)$, dominates both in the short- and long-wavelength limits. The terms related to $B^\pm(\omega)$ make essential contributions to $f_{\text{xc},ij}(q, \omega)$ only in the small ω region, where $A(\omega)$ vanishes as ω^2 .

The frequency-dependence of the LFF in the particle-hole continuum (PHC) region (finite

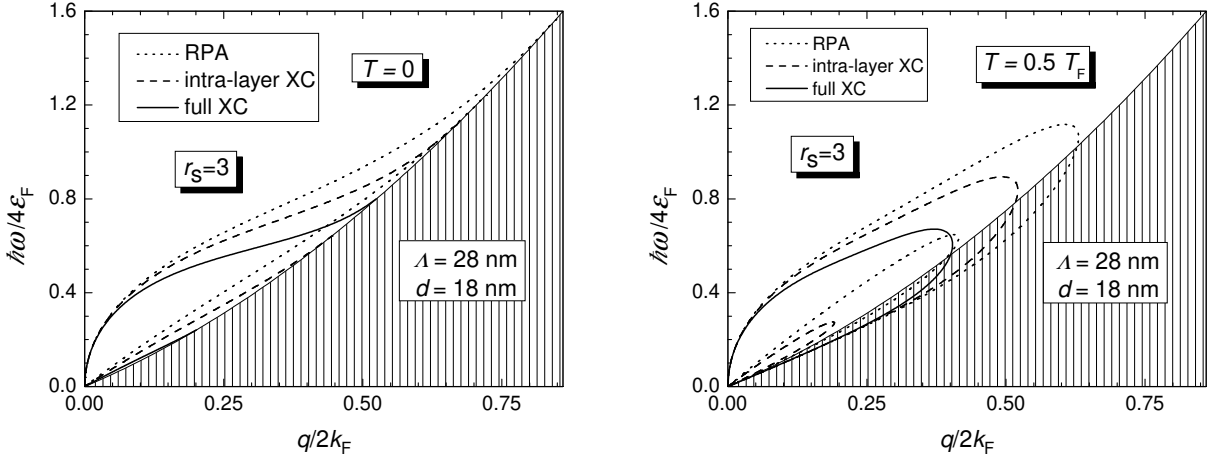


FIG. 4: Bilayer plasmon spectra at zero temperature (figure on the left) and at finite temperature, $T = 0.5T_F$ (figure on the right) for $r_s = 3$. The hatched area shows the PHC region at $T = 0$. The dispersions curves are calculated within the RPA (dotted curves) and beyond the RPA, taking into account the full intra- and inter-layer dynamic xc corrections (solid curves) or taking into account only the intra-layer dynamic xc effects (dashed curves).

wave vector, low frequency) is still largely unknown. For this reason, in evaluating the particle-hole contribution to the drag transresistivity, we use the static limit of the LFF. We take advantage of the analytical expressions recently obtained for $G_{\text{xc}}^-(q)$ and $G_{\text{xc}}^+(q)$, LFF³⁴, which accurately reproduce the diffusion Monte Carlo data³⁵, as well as the exact asymptotic behaviors in the large and small q limits. Notice that both the dynamic xc kernels^{30,31} and the static LFF³⁴, which we have used in our calculations, are evaluated at $T = 0$ in an ideal 2DES. At present there are no better approximations for the xc LFF in the literature, which include the finite temperature effect in a quasi-2DES. Recalculating the LFF at finite T and for finite width of layers, at the same level of sophistication as the LFF obtained so far, would be a major research project, well beyond the scope of this paper. We expect, however, that the finite temperature effects, which come from the higher order diagrams, should be weaker and play a minor role than the temperature dependence due to the Fermi factors and the non-interacting polarization function. Thus, as a first step in this direction we have used the $T = 0$ forms of the LFF and adopted an approach where the finite width effects affect the xc kernels in exactly the same way as they affect the bare Coulomb interaction, i.e. via form factors F_{ij} in Eq. 11.

In Fig. 3 we plot the intra- and inter-layer LFF $G_{\text{xc},ij}(q)$ which we actually use in our

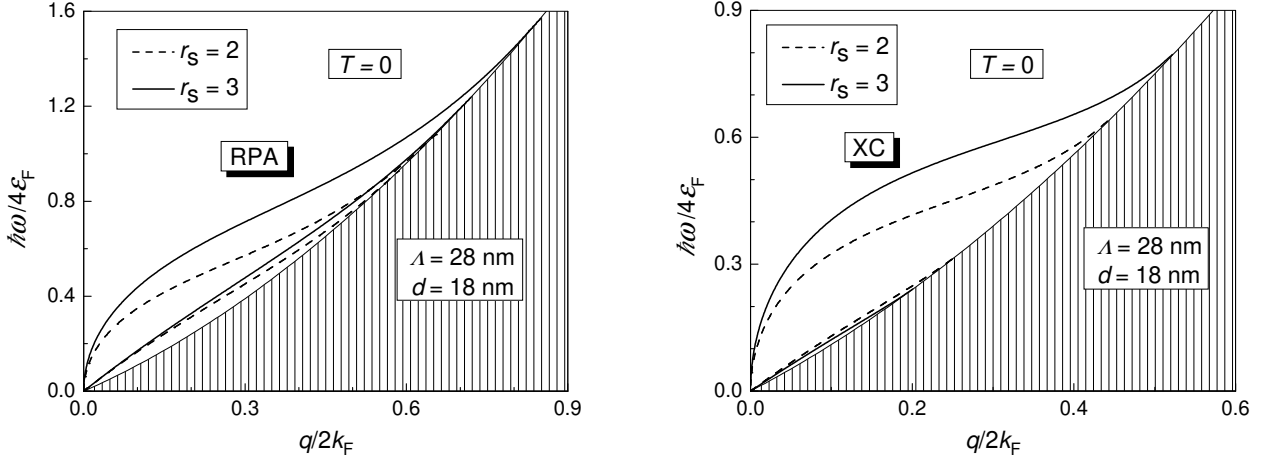


FIG. 5: Bilayer plasmon spectra at zero temperature. The hatched area shows the PHC region at $T = 0$. The dispersion curves are calculated within the RPA (figure on the left) and beyond the RPA by taking into account the effects of intra- and inter-layer dynamic xc (figure on the right). The solid and dashed curves correspond to the values of $r_s = 2$ and 3, respectively.

calculations of the drag transresistivity in the PHC region. For all the values of r_s shown in the figure, the intra-layer LFF $G_{xc,11}(q)$ become close to unity when $x = q/2k_F \lesssim 1$. Notice that in this region $G_{xc,11}(q)$ is significantly larger than the LFF in the Hubbard approximation, $G_H(x) = x/\sqrt{1 + 4x^2}$. This makes the effective intra-layer interaction weak in the region near $x = 1$ and results in a weak in-plane screening effect. This effect becomes especially important in the regime of low density bilayers where the main contribution to drag comes from the large-angle scattering processes with $x \lesssim 1$. From Fig. 3 we also see that although $G_{xc,12}(q)$ is smaller than $G_{xc,11}(q)$, the two LFF are of the same order of magnitude.

IV. BILAYER PLASMON DISPERSIONS: EFFECT OF DYNAMIC XC

Below we consider the symmetric bilayer 2DES ($n_1 = n_2$) with inter-layer spacing $\Lambda = 28$ nm and quantum wells width $d = 18$ nm, which correspond to the experimental situation in Ref. 8.

In this section we calculate the spectrum of bilayer plasmons for $r_s = 2$ and 3 both within the RPA and beyond it taking into account the dynamic xc effects through the intra- and inter-layer xc kernels. In the symmetric systems the bilayer screening function is represented

as

$$\varepsilon_{\text{bi}}(q, \omega) = \varepsilon_+(q, \omega)\varepsilon_-(q, \omega) , \quad (18)$$

where

$$\varepsilon_{\pm}(q, \omega) = 1 + V_{\pm}(q, \omega)\Pi^0(q, \omega) , \quad (19)$$

with $V_{\pm}(q, \omega) = V_{\text{eff},11}(q, \omega) \pm V_{\text{eff},12}(q, \omega)$. The spectrum of the collective excitations is obtained from the zeros of the real part of the bilayer screening function so the dispersion is obtained from the solution of the equation

$$\text{Re } \varepsilon_{\pm}(q, \omega_{\text{op,ac}}(q)) = 0 . \quad (20)$$

The imaginary part of the screening function describes the damping of the collective modes. In this approach the imaginary parts of the dynamic xc kernels are finite at finite frequencies and we obtain that even at zero temperature the collective excitations are Landau-damped outside the $T = 0$ PHC region. Also, we use the finite temperature forms for the polarization function $\Pi^0(q, \omega)$ which itself has a twofold effect on the plasmon spectrum. The finite temperature contribution to the imaginary part of $\Pi^0(q, \omega)$ outside the $T = 0$ PHC region enhances the damping of the collective modes, while temperature-induced changes in the real part of $\Pi^0(q, \omega)$ modify the domain of existence of the collective excitations.

In Fig. 4 we plot the plasmon spectra at zero and finite temperatures for $r_s = 3$, based on the above Eq. (20). The spectra are calculated within the RPA and in the approximations where only the intra-layer charge-charge xc kernels and the full intra- and inter-layer xc kernels are taken into account. The upper lying "optical" branches in all these approximations exhibit the expected square-root $\sim \sqrt{q}$ dispersion in the long wavelength limit, while the lower lying "acoustical" branches have linear $\sim q$ dispersion. The inclusion of the non-diagonal dynamic xc kernels forces both the optical and acoustical branches to enter the PHC at smaller values of q . As a result the acoustical branch stops to exist at finite temperatures when both the intra- and inter-layer xc effects are included. At finite T the group velocity of each type of plasmon, independently of the approximation used, becomes infinite at the upper edge of the wave vector interval in which the collective excitations exist.

Fig. 5 shows that, as the electron density decreases, both the optical and the acoustical plasmon dispersions, calculated within the RPA, move away from the boundary of the PHC. We find, however, that the many-body effects beyond the RPA result in a new tendency,

namely, the optical and the acoustical modes repel each other when r_s increases so that the acoustical branch becomes closer to the boundary of the PHC while the optical branch is still pushed away from it. As we see below all these changes, induced by the dynamic many-body effects, are directly reflected in the temperature dependence of the plasmon-mediated Coulomb drag.

V. DRAG TRANSRESISTIVITY WITHIN THE RPA

First we present the RPA based calculations of the drag due to the exchange of plasmons in low-density bilayers. In Fig. 6 the transresistivity (scaled by the factor $(T/T_F)^2$) is plotted as a function of temperature for three different densities corresponding to $r_s = 2, 3$ and 5 . Although the magnitude of the drag transresistivity increases with r_s , it is seen that within the RPA the qualitative behavior of the plasmon-mediated drag does not undergo strong changes when the electron density decreases, and it resembles the behavior at high densities²¹. The behavior of the transresistivity versus temperature exhibits an upturn at low temperatures near $0.2T_F$ and a plasmon enhancement peak at higher temperatures. At low temperature the transresistivity decreases slightly with decreasing density. In contrast to this, at high temperatures the height of the transresistivity peak increases approximately linearly with r_s in the range $2 < r_s < 5$. As seen in Fig 6 both the upturn temperature of the plasmon-mediated drag and the position of the plasmon enhancement peak increase with r_s . This is consistent with the above discussion of the plasmon spectra, since in the RPA the plasmon dispersion curves for both modes move away from the PHC when the density decreases. Notice, however, that the absolute value of the upturn temperature and the position of the plasmon-enhancement peak show opposite tendency and decrease with r_s . This is due to the fact that the Fermi temperature, T_F , decreases by a factor of 6.25 when r_s increases from 2 to 5.

In Fig. 7 we plot the total transresistivity, due to exchange of both plasmons and particle-hole excitations. against the part of the transresistivity that is due only to exchange of particle-hole excitations within the RPA. One can see that for $r_s = 2, 3$ and 5 when the density decreases, the contribution to the drag, made by particle-hole excitations, increases faster than the plasmon contribution to drag. However, the plasmon contribution remains essential in all three cases and results in the plasmon enhancement peaks, clearly seen in

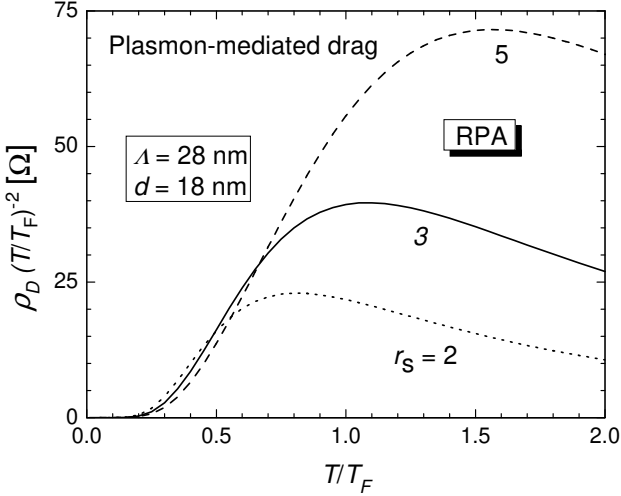


FIG. 6: Plasmon-mediated drag transresistivity as a function of scaled temperature within the RPA. The dotted, solid, and dashed curves correspond, respectively, to $r_s = 2$, 3 , and 5 .

the behavior of the scaled transresistivity versus temperature.

The dotted and dashed-dotted curves in Fig. 7 reproduce, respectively, the calculations by Zheng and MacDonald of the particle-hole contribution to the transresistivity³⁶ and by Flensberg and Hu of the plasmon-enhanced drag²¹ in the RPA. These curves correspond to the situation of the first drag experiment³⁷ on samples with high density, $n = 1.5 \times 10^{11} \text{ cm}^{-2}$, and large center-to-center inter-layer spacing, $\Lambda = 37.5 \text{ nm}$. Notice that the plasmon enhancement peak is most pronounced in Fig. 7. However, this strong effect is mainly caused by the large inter-layer separation which exceeds significantly the effective spacing of the bilayers in the experiment in Ref. 8 for which the solid lines are calculated. As far as the plasmon-mediated drag depends more weakly on inter-layer spacing than the particle-hole contribution to drag²¹, the plasmon enhancement peak is more pronounced for the dotted curves.

VI. DRAG TRANSRESISTIVITY BEYOND THE RPA

1. The effect of dynamic xc on plasmon-mediated drag

We include the intra- and inter-layer dynamic xc both within the schemes (8) and (15) and study their effect on the plasmon-mediated drag by comparing the obtained results with those of RPA-based calculations. In Figs. 8 and 9 the scaled transresistivity as a function

of temperature is shown for two equal density bilayer systems with $r_s = 2$ and 3. It is seen that the upturn temperature in the scaled transresistivity essentially decreases when the xc effects are included. Despite slight differences, in both cases the plasmons begin to contribute heavily to the inter-layer e-e interaction at temperatures about $0.1T_F$. Whereas, according to the RPA calculation, the upturn of the plasmon-mediated drag should be about $0.2T_F$. This difference is explained by the changes in the spectrum of bilayer plasmons induced by the dynamic xc effects and discussed in the previous section. At low temperature the plasmon-mediated drag is mainly determined by the acoustical plasmons, whose frequency is reduced by the dynamic xc: this makes the acoustic plasmons easier to excite thermally, and causes their contribution to the Coulomb drag to be larger than in RPA.

When temperature increases, the average energy of plasmons that mediate the drag increases. Hence, the plasmon damping, caused by dynamic xc effects, becomes stronger with a consequent reduction in the drag transresistivity. Thus, around $0.4T_F$ the plasmon-mediated drag obtained within the RPA exceeds the drag which takes into account the xc effects in the scheme (15). However, the plasmon-mediated drag calculated within the scheme (8) remains greater than that the one calculated within the RPA at all temperatures.

At still higher temperatures the plasmon-mediated drag shows a broad peak in the all approximations. The position of this peak is determined mainly by the position of the optical plasmons insofar as at such high temperatures the acoustical plasmons are heavily damped and merged into the PHC. As seen from Figs. 8 and 9 the peak position is at higher temperature at the lower density, and it changes slightly depending on the chosen approximation. These observations are again consistent with the behavior of the plasmon spectra in Figs. 4 and 5. The main contribution to the plasmon-mediated drag is made by the plasmons with energies $\hbar\omega \sim T$ while the scaled transresistivity peaks occur at temperatures $T \lesssim T_F$. Therefore, as seen in Figs. 4 and 5, at such small values of $\hbar\omega/4\epsilon_F \lesssim 0.25$, the positions of the optical plasmons, and hence the positions of the peak in the plasmon contribution to drag in Figs. 8 and 9, remain approximately unaffected. Notice also that at even higher temperatures the differences in the magnitude of plasmon-mediated drag in the different approximations diminishes with increasing T .

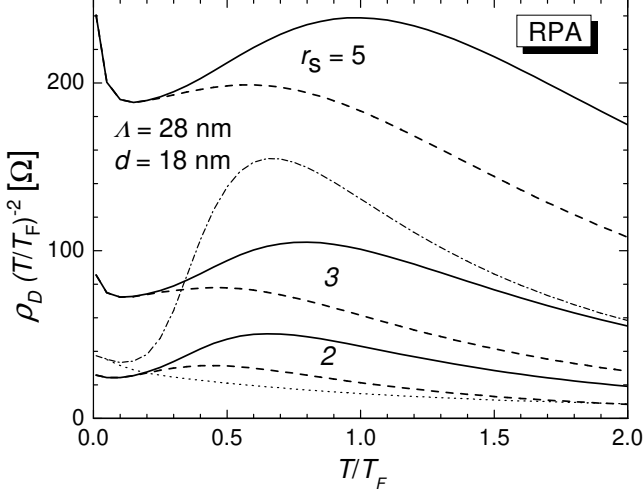


FIG. 7: Coulomb drag transresistivity as a function of scaled temperature within the RPA for $r_s = 2, 3$, and 5 . The solid curves correspond to the total drag, mediated both by plasmon and by particle-hole excitations, while the dashed curves represent only the particle-hole contribution. The dashed-dotted and dotted curves are for the situation corresponding to the first drag measurements of Ref. 37: they are rescaled by a factor of 20, and represent, respectively, the total drag and the drag due to exchange of particle-hole excitations only.

2. The combined effect of dynamic and static xc on the total drag

In this subsection we investigate the combined effect of the dynamic and static many-body xc on the total drag, mediated both by plasmon and by particle-hole excitations. We find that the static many-body LFF enhance strongly the particle-hole contribution to drag so that at low temperatures the total transresistivity within the scheme (8) overestimates by an order of magnitude the experimental findings in Ref. 8 as well as the drag rate obtained within the scheme (15). Therefore, for the total transresistivity we present only the results of the calculation within the latter scheme.

In Fig. 10 the drag transresistivity is plotted vs temperature within and beyond the RPA for $r_s = 2$. It is seen that in both approximations the particle-hole contribution to the scaled drag transresistivity first shows a slight dip followed by a peak at higher temperatures. In the RPA the plasmon contribution to drag enhances this peak and shifts it to even higher temperatures so that the total transresistivity shows a pronounced peak approximately at the position where the plasmon contribution has a peak. As seen from Fig. 10 the introduction of the static exchange-controlled LFF increases the peak height of

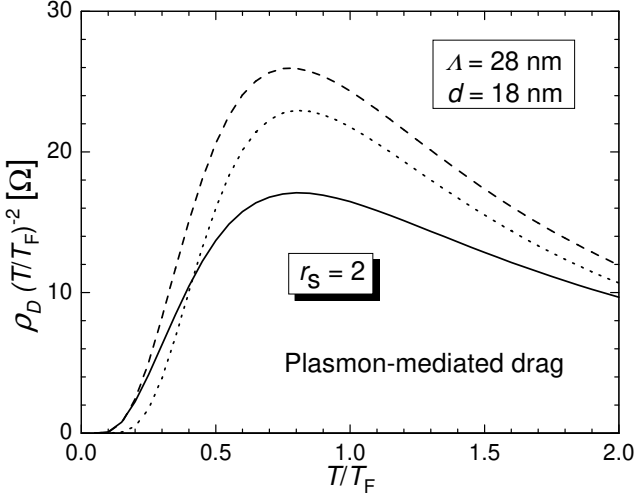


FIG. 8: Dynamic xc corrections to the plasmon-mediated drag for $r_s = 2$. The scaled transresistivity versus temperature is shown within the RPA (dotted curve) and beyond the RPA taking into account the intra- and inter-layer xc kernels within the scheme (15) (solid curve) and the scheme (8) (dashed curve).

the particle-hole contribution to the drag and shifts the peak towards lower temperatures. On the other hand, the plasmon-mediated drag is moderately suppressed by the dynamic xc corrections as discussed in the previous subsection (cf. Fig. 8). Thus, the resulting peak in the graph of the total transresistivity vs temperature remains a small feature at relatively low temperatures, while at high temperatures the drag rate shows a monotonic decrease in T .

The described quantitative and qualitative differences in the behavior of the scaled total transresistivity within and beyond the RPA becomes more pronounced at lower densities. As seen from Fig. 11 for $r_s = 3$ the total transresistivity beyond the RPA as a function of temperature shows no peak at all and this is in stark contrast to the peaked behavior of the transresistivity within the RPA. The disappearance of the large high-temperature plasmon peak results from the strong increase of the drag transresistivity at low temperatures: we ascribe this to the fact that the contribution to drag, made by large-angle inter-layer scattering processes, becomes dominant when the many-body xc corrections are included.

As shown recently in Ref. 8, the large-angle scattering processes with $q \simeq 2k_F$ play an important role in the Coulomb drag in low density bilayers. In such samples with sufficiently small inter-layer separations, $k_F\Lambda$ is so small that the usual exponential cutoff, $\exp(-q\Lambda)$, of the inter-layer e-e interaction is no longer effective in suppressing the large-angle scattering

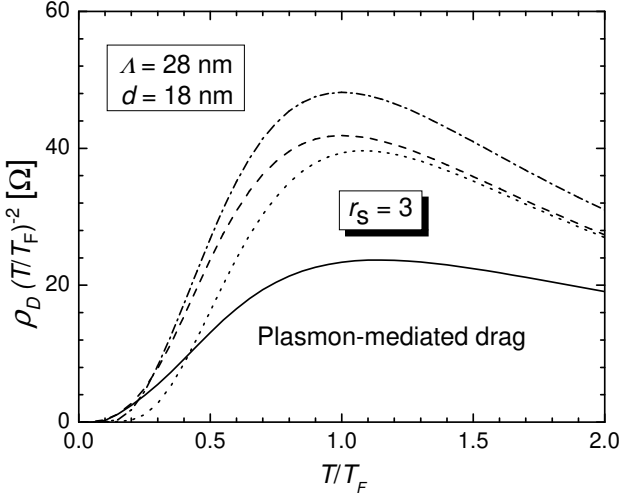


FIG. 9: Dynamic xc corrections to the plasmon-mediated drag for $r_s = 3$. The scaled transresistivity vs temperature is shown within the RPA (dotted curve) and beyond the RPA taking into account the intra- and inter-layer xc effects within the scheme (15) (solid curve) and the scheme (8) (the dashed). The dash-dotted curve corresponds to the calculations within the scheme (8) and accounts only for the intra-layer dynamic xc correction.

processes. Thus, according to previous predictions³⁸, the large-angle inter-layer scattering events, due to the divergence of the scattering phase-space near $q \simeq 2k_F$, lead to a $T^2 \ln T$ behavior of the drag transresistivity at low temperatures, in lieu of the usual T^2 temperature dependence, which is driven by small-angle scattering processes. To distinguish clearly the contributions to the drag made by the small- and large-angle inter-layer scattering processes, in Fig. 12 we have plotted the dimensionless drag intensity, $I(x)$, within and beyond the RPA versus the average transferred momentum, $x = q/2k_F$, at low temperature $T = 0.05T_F$. We have normalized the drag intensity to its corresponding peak values, ρ_p , so that the transresistivity $\rho_D = \rho_p \int I(x)dx$. It is evident that the xc effects reduce essentially the component from the small-angle scattering processes so that the large-angle scattering contribution dominates the drag. Thus, the drag rate is strongly enhanced at low temperatures owing to the logarithmic corrections provided by the large-angle scattering events. By contrast, in the RPA the contribution of the small-angle scattering processes remains dominant down to the lowest temperatures (see Fig. 12).

Lack of experimental measurements of the Coulomb drag at high temperatures does not allow for the time being an experimental verification of our predictions on the position and strength of the plasmon peak in low density bilayers. Notice however that at low

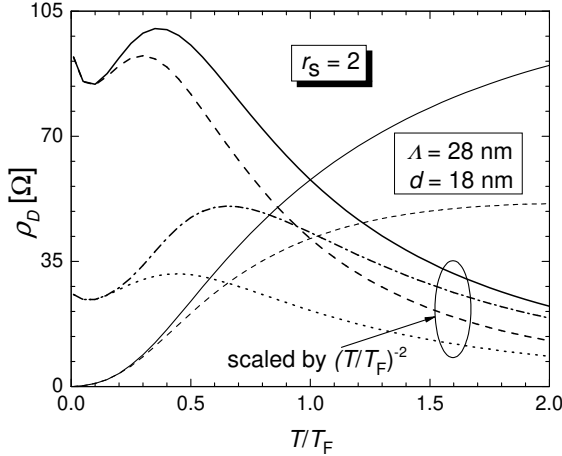


FIG. 10: The drag transresistivity vs temperature for $r_s = 2$. The solid and dashed curves represent the total transresistivity and the separate particle-hole contribution to the drag transresistivity with the full intra- and inter-layer xc corrections included within the scheme (15). The dash-dotted and dotted curves are, respectively, the total transresistivity and the particle-hole contribution to the drag calculated within the RPA.

temperatures, as shown in Fig. 13, our numerical results are in reasonable agreement with the experimental findings by Kellogg *et al.*⁸ for $n = 3.8 \times 10^{10} \text{ cm}^{-2}$ which is slightly higher than the density, $n = 3.69 \times 10^{10} \text{ cm}^{-2}$, used in our calculations for $r_s = 3$.

VII. SUMMARY

In this paper we have investigated the role of the many-body xc effects in the frictional Coulomb drag in low density bilayer 2DES. We have calculated the spectrum of the bilayer plasmons and the temperature dependence of the drag transresistivity in a broad range of temperatures. Our calculations include both intra- and inter-layer xc effects. These effects are critical in low density bilayers since the inter-layer separation in these structures is comparable with the inter-particle spacing in an individual 2DES. We have proposed a new approach and employed the full dynamic xc kernels of the bilayer 2DES in calculations of the acoustical and optical plasmon dispersions as well as in the drag, mediated by exchange of bilayer plasmons. In studying the many-body effects on the particle-hole contribution to drag we have still used the static exchange-controlled LFF. The combined effect of the dynamic and static many-body xc on drag has been investigated in comparison with RPA-based calculations of the transresistivity vs temperature for different values of the electron

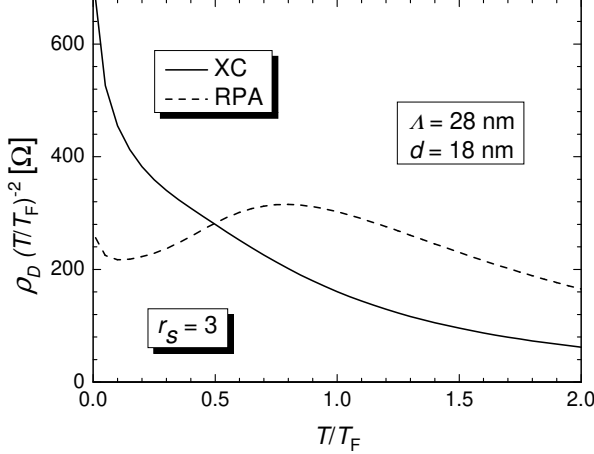


FIG. 11: The full many-body corrections to the total transresistivity for $r_s = 3$. The dashed and solid curves represent the scaled transresistivity vs temperature, calculated, respectively, within and beyond the RPA. The intra- and inter-layer xc corrections are included within the scheme (15). The RPA data are multiplied by a factor of 3.

density.

We have observed that after the inclusion of the full dynamic xc kernels, a decrease of the electron density induces shifts of the plasmon branches in opposite directions. And this is in stark contrast to the tendency obtained within the RPA that both optical and acoustical plasmons move away from the boundary of the PHC with a decrease of the electron density. In the presence of the xc effects, the optical mode still moves away from the PHC while the acoustical branch moves closer to the PHC. The effect is so strong that at $r_s = 3$ the acoustical branch enters the PHC and becomes completely destroyed at finite temperatures. These changes of the plasmon spectrum, induced by the intra- and inter-layer dynamic xc, are reflected in the temperature dependence of the plasmon-mediated drag. The upturn temperature strongly decreases so the bilayer plasmons heavily contributes to the drag starting at temperatures $0.1T_F$, which is approximately a factor of 2 small than the upturn temperature calculated within the RPA for $r_s = 2$. The effect becomes slightly stronger for $r_s = 3$.

At fixed electron density the dynamic xc correction reduces the frequency of both plasmon modes in comparison with the RPA-based results. However, the changes in the spectrum of the optical mode are pronounced only at large wave vectors and high frequency. At the relatively high temperatures, which are necessary to thermally excite these optical modes,

the strong Landau damping weakens the plasmon contribution to drag. Therefore, we have found that the "redshift" of the plasmon-mediated drag peak, induced by the dynamic xc effects, is relatively weak. Our results show that at low temperatures the dynamic xc effects enhance the plasmon-mediated drag while at high temperatures they have the opposite effect. We ascribe this to the enhancement of the damping of high energy plasmons, caused by dynamic many-body xc effects.

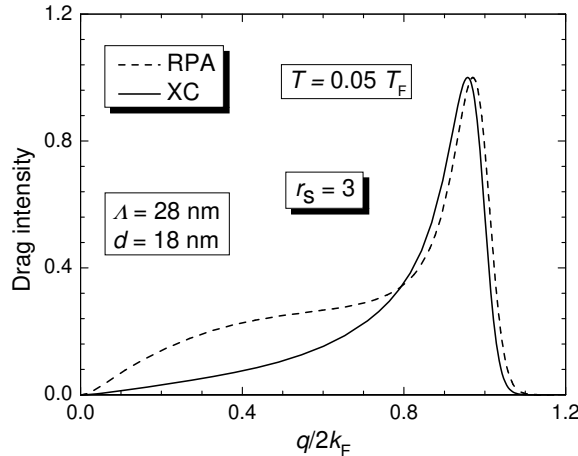


FIG. 12: Drag intensity $I(x)$ as a function of transferred momentum $x = q/2k_F$ for $r_s = 3$. The solid and dashed curves represent respectively the results of calculations within and beyond the RPA at $T = 0.05T_F$. The respective values of the drag transresistivity in Fig. 11 are given by the area under these curves. The curves are normalized to their particular peak values, $\rho_p = 241.02$ and 2291.92Ω .

The combined effect of the dynamic and the static many-body xc in low density bilayers results in both quantitative and qualitative changes in the behavior of the drag transresistivity. At temperatures near $0.5T_F$ the transresistivity with the xc effects included is larger approximately by a factor of 3 than that obtained within the RPA for $r_s = 3$. The enhancement increases strongly at low temperatures where the drag is dominated by large-angle scattering processes with $q \simeq 2k_F$. We have found that the plasmon enhancement peak, which is clearly seen in the RPA based calculations, disappears after the full xc corrections have been introduced. The disappearance of the large high-temperature plasmon peak is the result of the strong enhancement of the particle-hole contribution to drag at low temperatures and of the moderate suppression of the plasmon-mediated drag at high temperatures when, respectively, the full static and dynamic xc corrections are included. We have ascribed

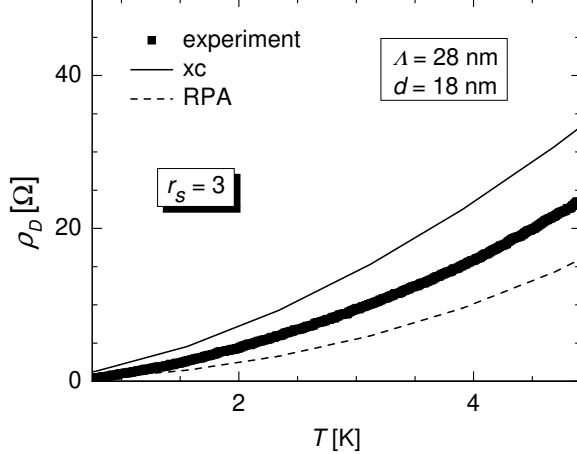


FIG. 13: The transresistivity vs temperature for $r_s = 3$. The intra- and inter-layer many-body corrections are included within the scheme (15) (the solid curve). The RPA data (the dashed curve) are multiplied by a factor of 2. The symbols are the experimental findings from Ref. 8 for $n = 3.8 \cdot 10^{10} \text{ cm}^{-2}$.

this behavior to the change in the specific contributions to drag made by small- and large-angle scattering events. Our calculations demonstrate clearly that the xc effects increase the large-angle scattering component of the drag making it the dominant contribution. This component strongly enhances the drag for two reasons. First, at low temperatures the e-e scattering phase-space diverges near $x = q/2k_F \simeq 1$. On the other hand, when $x \simeq 1$, the static intra-layer LFF $G_{11}(x)$ becomes close to unity, leading to a reduction of the effective intra-layer interaction $V_{\text{eff},11}(x)$. This by itself weakens the dynamic intra-layer screening and enhances the drag. Thus, on the background of the large transresistivity at small T , the plasmon-mediated contribution to drag does not result in a peaked behavior of the scaled transresistivity and the total drag rate decreases monotonically in T . In the RPA, the drag still contains a strong small-angle scattering component which suppresses partially the enhancement at small T and the plasmon peak remains visible.

Our numerical results are in reasonable agreement with the experimental findings by Kellogg *et al.*⁸. Currently, the available experimental data for the low density electron samples are restricted to low temperatures where the plasmon contribution to drag is small. An experimental verification of the plasmon peak disappearance requires new drag measurements in low density electron bilayers in a broad range of temperatures close to T_F .

Acknowledgments

We thank Zhixin Qian for kindly making the results of his calculations accessible prior to publication. This work was supported by the Korea Science and Engineering Foundation Grant No. R05-2003-000-11432-0, by the Ministry of Science and Education of Armenia Grant No. 0127, by a DAAD technical grant, and by the US Department of State. G.V. acknowledges support from NSF Grant No. DMR-0313681.

* Also at: Radiophysics Department, Yerevan State University, Yerevan, 375025 Armenia; Electronic address: badalyan@yerphi.am

¹ *Perspectives in Quantum Hall Effects*, edited by S. Das Sarma and A. Pinczuk (Wiley, New-York, 1997), chapters by S.M. Girvin and A.H. MacDonald and by J.P. Eisenstein.

² J.P. Eisenstein and A.H. MacDonald, cond-mat/0404113.

³ M. B. Pogrebinskii, Sov. Phys. Semicond. **11**, 372 (1977); P. J. Price, Physica **117 & 118**, 750 (1983).

⁴ A. Rojo, J. Phys.: Condens. Matter **11**, R31 (1999).

⁵ *Quantum Theory of the Electron Liquid*, G. F. Giuliani and G. Vignale, (Cambridge University Press, Cambridge, 2005), Chapter 10.

⁶ R. Pillarisetty, Hwayong Noh, D. C. Tsui, E. P. De Poortere, E. Tutuc, and M. Shayegan, Phys. Rev. Lett. **89**, 016805 (2002).

⁷ R. Pillarisetty, Hwayong Noh, E. Tutuc, E. P. De Poortere, K. Lai, D. C. Tsui, and M. Shayegan, Phys. Rev. B **71**, 115307 (2005).

⁸ M. Kellogg, J. P. Eisenstein, L. N. Pfeiffer, and K. W. West, Solid State Commun. **123**, 515 (2002).

⁹ A.-P. Jauho and H. Smith, Phys. Rev. B **47**, 4420 (1993).

¹⁰ T. J. Gramila, J. P. Eisenstein, A. H. MacDonald, L. N. Pfeiffer, and K. W. West, Phys. Rev. B **47**, 12 957 (1993).

¹¹ H Rubel, E H Linfield, D A Ritchie, K M Brown, M Pepper and G A C Jones, Semicond. Sci. Technol. **10**, 1229 (1995).

¹² H. Noh, S. Zelakiewicz, T. J. Gramila, L. N. Pfeiffer and K. W. West, Phys. Rev. B **59**, 13 114

(1999).

¹³ C. Jörger, S. J. Cheng, W. Dietsche, R. Gerhardts, P. Specht, K. Eberl and K. von Klitzing, *Physica E* **6**, 598, 2000.

¹⁴ H. C. Tso, P. Vasilopoulos, and F. M. Peeters, *Phys. Rev. Lett.* **68**, 2516 (1992).

¹⁵ M. Chr. Bønsager, K. Flensberg, Ben Yu-Kuang Hu, and A. H. MacDonald, *Phys. Rev. B* **57**, 7085 (1998). [15]

¹⁶ S. M. Badalyan and U. Roessler, *Phys. Rev. B* **59**, 5643 (1999).

¹⁷ U Sivan, P. M. Solomon, and H. Shtrikman, *Phys. Rev. Lett.* **68**, 1196 (1992).

¹⁸ N. P. R. Hill, J. T. Nicholls, E. H. Linfield, M. Pepper, D. A. Ritchie, G. A. C. Jones, Ben Yu-Kuang Hu, and Karsten Flensberg, *Phys. Rev. Lett.* **78**, 2204 (1997);

¹⁹ H. Noh, S. Zelakiewicz, X. G. Feng, T. J. Gramila, L. N. Pfeiffer, and K. W. West, *Phys. Rev. B* **58**, 12 621 (1998).

²⁰ H. C. Tso, P. Vasilopoulos, and F. M. Peeters, *Phys. Rev. Lett.* **70**, 2146 (1993).

²¹ K. Flensberg and Ben Yu-Kuang Hu, *Phys. Rev. Lett.* **73**, 3572 (1994); *Phys. Rev. B* **52**, 14796 (1995).

²² L. Świerkowski, J. Szymański, and Z. W. Gortel, *Phys. Rev. Lett.* **74**, 3245 (1995); *Phys. Rev. B* **55**, 2280 (1997).

²³ E. H. Hwang, S. Das Sarma, V. Braude, and A. Stern, *Phys. Rev. Lett.* **90**, 086801 (2003).

²⁴ A. Yurtsever, V. Moldeveanu, and B. Tanatar, *Solid State Commun.* **125**, 575 (2003).

²⁵ F. von Oppen, S. H. Simon, and A. Stern, *Phys. Rev. Lett.* **87**, 106803 (2001); B. N. Narozhny, I. L. Aleiner, and A. Stern, *Phys. Rev. Lett.* **86**, 3610 (2001).

²⁶ P. F. Maldague, *Surf. Sci.* **73**, 296 (1978).

²⁷ G. Vignale and K. S. Singwi, *Phys. Rev. B* **31**, 2729 (1985); *ibid* **32**, 2156 (1985).

²⁸ L. Zheng and A. H. MacDonald, *Phys. Rev. B* **48**, 8203 (1993).

²⁹ D. Yoshioka, A. H. MacDonald, and S. M. Girvin, *Phys. Rev. B* **39**, 1932 (1989).

³⁰ Z. Qian and G. Vignale, *Phys. Rev. B* **65**, 235121 (2002).

³¹ Z. Qian, preprint.

³² Z. Qian, A. Constantinescu, and G. Vignale, *Phys. Rev. Lett.* **90**, 066402 (2003).

³³ A. Holas and K. S. Singwi, *Phys. Rev. B* **40**, 158 (1989); A. J. Glick and W. F. Long, *Phys. Rev. B* **4**, 3455 (1971).

³⁴ B. Davoudi, M. Polini, G. F. Giuliani, and M. P. Tosi, *Phys. Rev. B* **64**, 153101 (2001); *ibid*

64, 233110 (2001).

³⁵ G. Senatore, S. Moroni, and D. M. Ceperley, in *Quantum Monte Carlo methods in Physics and Chemistry*, edited by M. P. Nightingale and C. J. Umrigar, Kluwer, Dordrecht, 1999.

³⁶ L. Zheng and A. H. MacDonald, Phys. Rev. B **48**, 8203 (1993).

³⁷ T. J. Gramila, J. P. Eisenstein, A. H. MacDonald, L. N. Pfeiffer, and K. W. West, Phys. Rev. Lett. **66**, 1216 (1991).

³⁸ C. Hodges, H. Smith, and J. W. Wilkins, Phys. Rev. B **4**, 302 (1971).